Taylor & Francis
Taylor & Francis Group

Advanced Composite Materials

ISSN: 0924-3046 (Print) 1568-5519 (Online) Journal homepage: http://www.tandfonline.com/loi/tacm20

Investigation about the fracture behavior and strength in a curved section of CF/PP composite by a thin-curved beam specimen

Tsuyoshi Matsuo, Takeshi Goto & Jun Takahashi

To cite this article: Tsuyoshi Matsuo, Takeshi Goto & Jun Takahashi (2015) Investigation about the fracture behavior and strength in a curved section of CF/PP composite by a thin-curved beam specimen, Advanced Composite Materials, 24:3, 249-268, DOI: 10.1080/09243046.2014.886754

To link to this article: http://dx.doi.org/10.1080/09243046.2014.886754

Published online: 13 Feb 2014.

Advanced Composite Materials, 2015
Vol. 24, No. 3, 249–268, http://dx.doi.org/10.1080/09243046.2014.886754

Investigation about the fracture behavior and strength in a curved section of CF/PP composite by a thin-curved beam specimen

Tsuyoshi Matsuo*, Takeshi Goto and Jun Takahashi

Department of Systems Innovation, School of Engineering, The University of Tokyo, 7-3-1 Hongo, Bunkyo-ku, Tokyo 113-8656, Japan

(*Received 5 September 2013; accepted 21 January 2014*)

A curved beam specimen with a curved section bent at a right angle and straight arms is an efficient experimental method to evaluate the interlaminar tensile strength of a composite laminate. This paper describes a technique to apply such a test method to determining the fracture behavior and strength in a curved section of a thin laminate. The proposed technique is capable of estimating appropriately the compressive or tensile strength as well as the interlaminar tensile strength at failure in a thin-curved section, especially targeting thermoplastic composite materials. The significant point of the proposed technique is a modified calculating method of the stress distribution in a curved section by taking into account the large deformation of the specimen because of thin laminate.

Keywords: curved beam specimen; thermoplastic composite; CF/PP; interlaminar tensile strength; compressive strength

1. Introduction

With the growth of the requirement of lightweight materials and structures, laminated composites have been developed and manufactured for a variety of applications. In particular, thermoplastic composite materials have been expected to be widely used in mass produced transportation sectors due to its high mechanical performance and lightweight effect. Especially, carbon fiber reinforced thermoplastic composite has a lot of advantages to enhance mechanical properties as represented by impact energy absorption as well as to achieve high-cycle and low-cost manufacturing technologies.[1] Polypropylene (PP) is one of thermoplastic polymers, and its high productivity and dramatic improvement of mechanical performance have attracted great attention on automotive applications, providing a wide range of usage.[2] Although there were some significant demerits about a combination of continuous carbon fiber (CF) and polypropylene, taking a few examples, in relation to the inadequate impregnation of PP and the low interfacial adhesive strength, some developed technologies have addressed those weak points and satisfied high performance of CF/PP composite.[3–5]

In keeping with this trend, the range of application of thermoplastic composite is spreading gradually, and a variety of shapes are being developed for designing structural member. Above all, a curved shape ranging from thin laminate to thick laminate is an important design factor to have key roles of structural components.

*Corresponding author. Email: matsuo@sys.t.u-tokyo.ac.jp

One of the important evaluated properties of the curved laminate is the out-of-plane property including the interlaminar tensile strength, which is closely related to the delamination in the curved section.[6–8] In previous researches, there have been a lot of attempts to develop test methods for measuring the out-of-plane properties.[9–14] For example, the uniaxial out-of-plane loading test was utilized to measure through the thickness strength of fiber reinforced plastics.[9,13] But, this method required a relatively thick (over 12 mm) specimen for achieving relatively consistent evaluation, and if using a relatively thin plate, test results showed significant scatter.[9] On the other hand, the test methods using a curved laminate itself have been developed to achieve validity for estimating the interlaminar tensile strength of the curved laminate,[10–12,14] and have been also applied to verifying the strain rate dependency of the out-of-plane property and the interface behavior between the skin and core of curved sandwich beam.[15,16] However, their methods made mention of only interlaminar tensile property in curved section. But in fact, a further thin-curved laminate has some possibility to generate not only the interlaminar failure but also the tensile or compressive failure on the curved surface.

The attempt of this study is to spread the range of application of the curved beam test method and make it possible to evaluate the tensile or compressive strength as well as the interlaminar tensile strength, in order for more practical usage of thin-curved laminate. A curved beam specimen with a section bent at right angle and straight arms, which is called L-shaped specimen, was utilized due to its relative ease of manufacture for thermoplastic composite laminate which consists of continuous carbon fiber and polypropylene. When using the L-shaped specimen, a four-point bending test has several advantages rather than a hinged loading tensile test because of a state of pure bending moment in the measured section,[11,14] which means no interlaminar shear stress. But in this study, one of valuable parameters is a tensile or compressive strength of the curved section of thin laminate. If using the four-point-bending test, there was a threat that some contacting stress concentration on a straight thin beam induces the first failure at each point where the specimen is loaded by cylindrical bars and the compressive failure in the curved section cannot be generated. In contrast, the tensile test does not have such a failure mode because there is no contacting stress.

Even if the interlaminar shear stress is possibly induced in the curved section while tensile loading, an appropriate stress analysis in the curved section can address a meaningful evaluation of the curved laminate properties, taking into account a large geometric deformation of the thin-curved beam. Finite element analysis supports the validation of such a stress analysis. This paper proposes a methodology for estimating the curved laminate properties of thin-curved beam specimen and discusses the fracture behavior and strength of the curved section.

2. Material-specification and experimental procedure

2.1. Materials

The developed composite material is CF/PP composed of surface-treated carbon fiber TR50S supplied by Mitsubishi Rayon and acid-modified polypropylene supplied by TOYOBO.[3–5] Figure 1 shows a roll of the prepreg tape with the polypropylene impregnated into the unidirectional bundle of the carbon fibers. The in-plane fiber-directional elastic modulus of the laminated CF/PP was determined by in-plane tensile experiments. And, the other material properties including the out-of-plane shear

Figure 1. Prepreg tape of carbon fiber and polypropylene.

modulus were estimated almost the same as theoretical values calculated from the rule of mixtures [17] or those properties of polypropylene itself.[3,5]

2.2. *Specimen manufacture*

The thin-curved beam specimen with the fibers aligned along the curved beam was manufactured by a heat-and-cool pressing technology, which is one of press molding techniques. Through the molding process, the stack of unidirectional prepreg tapes with the width of 15 mm was heated up to almost 200 °C in a set of upper and lower L-shaped molds as illustrated in Figure 2, after that, cooled down and compressive pressed around 160 °C with a pressure of 10 MPa on the material by hydraulically controlled pressing machine. The demolded final specimen as shown in Figure 3 has no significant spring back effects and was formed into the shape corresponding exactly to each inner geometry of the three sets of molds, with the same in width $b = 15$ mm, the

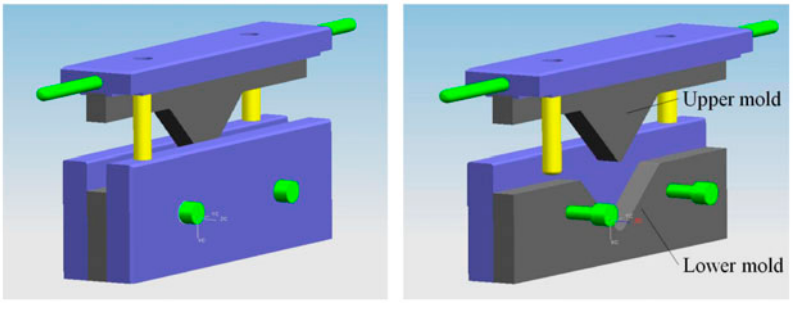

Figure 2. L-shaped molds – (left) the outer appearance (right) the inner geometry.

Figure 3. Thin-curved beam specimen with a magnified image of curved section.

same in thickness $t = 2$ mm, and the three different kinds of inner and outer radius, $r_i = 10$ mm and $r_o = 12$ mm, $r_i = 15$ mm and $r_o = 17$ mm, $r_i = 20$ mm and $r_o = 22$ mm, respectively. Accordingly, it can be assumed that the curved beam specimen has the orthotropic property along the tangential direction in the curved section. The material properties as explained in Table 1 were determined as follows:

$$E_\theta = 96.5 \text{ GPa} \quad E_r = 2.9 \text{ GPa} \quad \nu_{\theta r} = 0.26 \quad G_{\theta r} = 1.1 \text{ GPa}.$$

2.3. *Experimental setup and configuration*

The test configuration as shown and schematically illustrated in Figure 4 was determined by the geometry of the fixture. The test method used a universal testing machine Shimadzu AGS-5kNX using a 5kN load cell with a measuring accuracy of ±0.5% and a steel-hinged loading mechanism, which was aligned and clamped on to the specimen's loading arms. The dimensions and variables illustrated in Figure 5 are defined in Table 1. According to Figure 5, the setup parameters are as follows:

$$\text{initial } \phi_i = 45^\circ \quad d = 26 \text{ mm} \quad L = 45 \text{ mm}.$$

The tensile displacement was controlled at the speed of 1.0 mm/min during loading. The testing machine recorded loads and displacements digitally until the failure was observed on the specimen.

3. Analysis

3.1. *Theoretical stress solutions*

3.1.1. *Previous stress solutions*

Stress equations were developed by Lekhnitskii [18] for the stresses in a curved beam section with cylindrical anisotropy. And, based on the solutions, Shivakumar [19] and Hufenbach et al. [15] proposed a method for an analytical calculation of the radial and tangential stress distributions respectively in the curved section. In this analytical method, the applied tensile force F was translated to the ends of the curved section as illustrated in Figure 6(a) and (b), and the force translation results in two separated stress solutions for semicircular beam assuming two different loading cases with a pure end force F and a pure bending moment M at each end.

Based on these assumptions, the radial stress distribution $\sigma_r(r,\theta)$ and the tangential stress distribution $\sigma_\theta(r,\theta)$ in the curved section are produced respectively by the end force and the moment at the ends of the curved section as the following Equations (1)–(11).

Table 1. Symbolic definition.

Symbols	Definition
Material property	
E_θ	Young's modulus in the tangential direction
E_r	Young's modulus in the radial direction
$G_{\theta r}$	Shear modulus
$v_{\theta r}$	Poisson's ratio
Specimen geometry	
t, b	Specimen thickness and width
r_i, r_o	Specimen inner and outer radius
r_m	Specimen radius of the midplane
r, θ	Cylindrical coordinates of any point in the curved section
Experimental geometry	
d	Longitudinal distance of force application
L	Transversal distance of force application
ϕ	Angle of the loading arm from vertical
ϕ_i	Initial angle of ϕ
D_x	Horizontal distance between points of 'O' and 'B' (refer to Figure 5)
D_y	Vertical distance between points of 'O' and 'A' (refer to Figure 5)
D_a	Distance between points of 'B' and 'C' (refer to Figure 5)
Experimental measurement and calculation	
F, δ	Loading force and displacement
M	Moment applied by the lever L and the offset d
M^*	Additional moment applied by the integration of the tangential stress σ_θ to the end of the curved section
M_a	Accurate moment applied to the end of the curved section
σ_r	Radial stress at any coordinate in the curved section
σ_θ	Tangential stress at any coordinate in the curved section
σ_r^M	Radial stress by the moment M
σ_θ^M	Tangential stress by the moment M
σ_r^F	Radial stress by the end force F
σ_θ^F	Tangential stress by the end force F
σ_r^{Ma}	Radial stress by the accurate moment M_a
σ_θ^{Ma}	Tangential stress by the accurate moment M_a
k, c, g_M, g_F	Dimensionless constants
r_i', r_o'	Deformed inner and outer radius
r_m'	Deformed radius of the midplane
D_{xi}	Initial horizontal distance of D_x
D_{yi}	Initial vertical distance of D_y
ϕ'	Real angle of loading arm from vertical at point 'D', taking into account bending deflection of the arm (refer to Figure 16)
φ	Bending deflection angle of arm at point 'D' (refer to Figure 16)
σ_θ^C	Compressive strength in the tangential direction
σ_r^T	Interlaminar tensile strength in the radial direction

The analysis assumed a state of plane strain. The material variables are defined in Table 1 and the geometry variables are shown in Figures 5 and 6.

The radial stress distribution $\sigma_r^M(r,\theta)$ and the tangential stress distribution $\sigma_\theta^M(r,\theta)$ in the curved section under the pure bending moment M were derived as follows [11,18]:

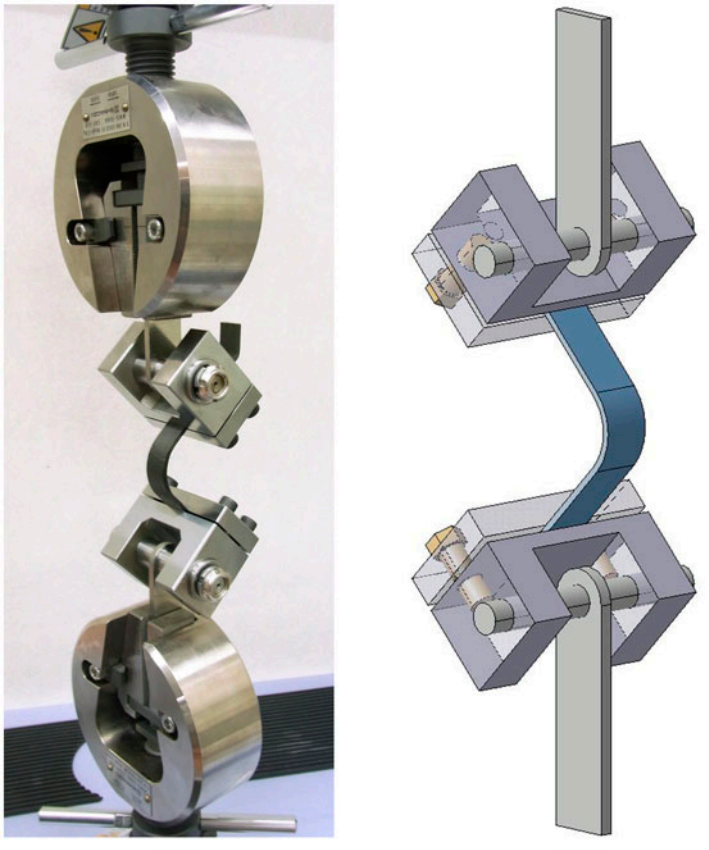

Figure 4. (a) Test assembly for experiments, (b) schematic figure of test configuration.

$$\sigma_r^M(r,\theta) = -\frac{M}{r_o^2 \cdot b \cdot g_M}\left\{1 - \frac{1-c^{k+1}}{1-c^{2k}} \cdot \left(\frac{r}{r_o}\right)^{k-1} - \frac{1-c^{k-1}}{1-c^{2k}} \cdot c^{k+1} \cdot \left(\frac{r_o}{r}\right)^{k+1}\right\}, \quad (1)$$

$$\sigma_\theta^M(r,\theta) = -\frac{M}{r_o^2 \cdot b \cdot g_M}\left\{1 - \frac{1-c^{k+1}}{1-c^{2k}} \cdot k \cdot \left(\frac{r}{r_o}\right)^{k-1} + \frac{1-c^{k-1}}{1-c^{2k}} \cdot k \cdot c^{k+1}\left(\frac{r_o}{r}\right)^{k+1}\right\}, \quad (2)$$

$$\text{where, } g_M = \frac{1-c^2}{2} - \frac{k}{k+1} \cdot \frac{(1-c^{k+1})^2}{1-c^{2k}} + \frac{kc^2}{k-1} \cdot \frac{(1-c^{k-1})^2}{1-c^{2k}}, \quad c = \frac{r_i}{r_o}, \; k = \sqrt{\frac{E_\theta}{E_r}}. \quad (3)$$

In Figure 6(b), the anisotropy pole is the origin of the coordinates, and the radius r is a coordinate value of any point in the curved section and ranges from the inner radius r_i to the outer radius r_o. And, the angle θ is a coordinate value of any point ranging from the end of the curved section to the other end. And, basically the end moment of the curved section was calculated by the addition of the moment by the loading arm length

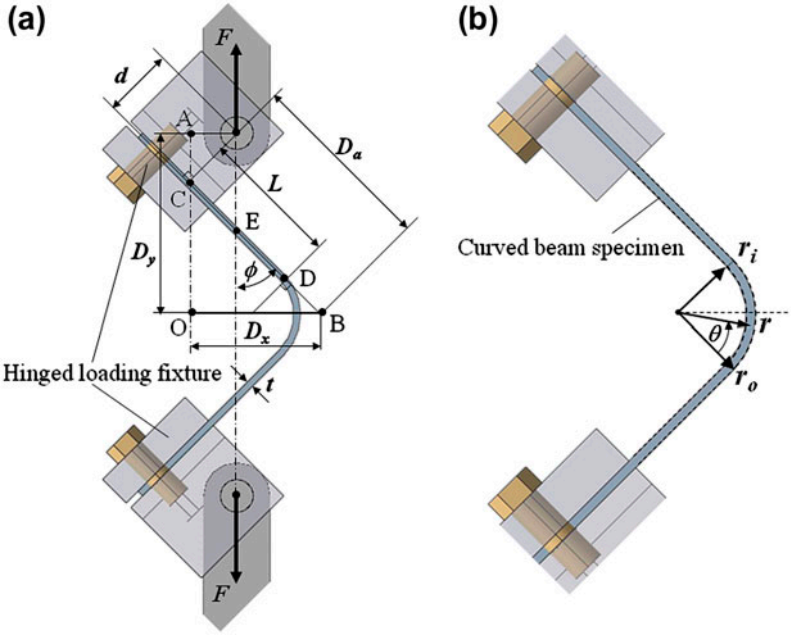

Figure 5. (a) Experimental setup with parameters used for the analysis, (b) Detail of the curved section.

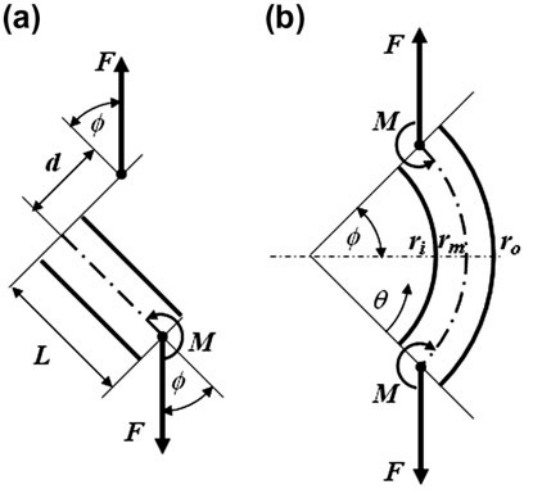

Figure 6. Geometry parameters of the specimen (a) lever and (b) curved beam section.

L and the moment by the offset d of the loading fixture from the neutral axis of the plate,

$$M = F \cdot (L \cdot \sin\phi - d \cdot \cos\phi). \tag{4}$$

On the other hand, the radial stress distribution $\sigma_r^F(r,\theta)$ and the tangential stress distribution $\sigma_\theta^F(r,\theta)$ only with the end force F were derived as follows [10,18]:

$$\sigma_r^F(r,\theta) = \frac{F}{b \cdot g_F \cdot r}\left\{\left(\frac{r}{r_o}\right)^\beta + c^\beta \cdot \left(\frac{r_o}{r}\right)^\beta - 1 - c^\beta\right\} \cdot \sin\left(\theta - \phi + \frac{\pi}{2}\right), \tag{5}$$

$$\sigma_\theta^F(r,\theta) = \frac{F}{b \cdot g_F \cdot r}\left\{(1+\beta) \cdot \left(\frac{r}{r_o}\right)^\beta + (1-\beta) \cdot c^\beta \cdot (\frac{r_o}{r})^\beta - 1 - c^\beta\right\} \cdot \sin\left(\theta - \phi + \frac{\pi}{2}\right), \tag{6}$$

$$\text{where, } g_F = \frac{2}{\beta} \cdot (1 - c^\beta) + (1 + c^\beta) \cdot \ln(c), \tag{7}$$

$$\beta = \sqrt{1 + \frac{E_\theta}{E_r} \cdot (1 - 2 \cdot \nu_{\theta r}) + \frac{E_\theta}{G_{\theta r}}}. \tag{8}$$

Additionally, Jackson et al. [10] proposed a correction to Lekhnitskii's end force solution to subtract out the additional moment M^* applied to the end of the curved section by the integration of the tangential stress σ_θ, and developed the expression for the moment M^* as the following,

$$M^* = \int_{r_i}^{r_o} \sigma_{\theta(\theta=0)} \cdot \left(r - \frac{r_i + r_o}{2}\right) \cdot b \cdot dr = \frac{F}{2} \cdot (r_i + r_o) \cdot \cos\phi. \tag{9}$$

So, the accurate moment M_a was derived as the following equation,

$$M_a = M - M^* = F \cdot (L \cdot \sin\phi - d \cdot \cos\phi - \frac{\mathrm{r_i} + \mathrm{r_o}}{2} \cdot \cos\phi). \tag{10}$$

From Equations (1)–(3) and (10), the radial and tangential stress distributions by the pure moment can be calculated by the replacement of M with M_a. From Equations (5)–(8), the radial and tangential stress distributions by the pure end force reaches a maximum at θ equals ϕ at any value of radius r. Consequently, by applying a superposition principle, the stresses expressed from Equations (1), (2), (5), and (6) result in the stress distribution related to the radial and tangential direction at the symmetry plane where θ equals ϕ as follows:

$$\sigma_r(r) = \sigma_r^{M_a}(r) + \sigma_r^F(r), \quad \sigma_\theta(r) = \sigma_\theta^{M_a}(r) + \sigma_\theta^F(r), \quad \text{where, } \theta = \phi. \tag{11}$$

3.1.2. *Proposed geometry modifications*

In this study, the effect of loading deformation is not negligible due to very thin specimen. The loading angle ϕ changes significantly during loading, and the specimen radius r_i, r_o and r_m also change with the angle between two loading arms spreading.

The following procedure is proposed to calculate ϕ, r_i', r_o', and r_m' at a certain displacement δ. The vertical distance D_y is obtained from the constant length D_a and d, and the variable angle ϕ of the deformed specimen as the following,

$$D_y = D_a \cdot \cos\phi + d \cdot \sin\phi. \tag{12}$$

Figure 5(a) shows this geometry relationship, and then the angle ϕ can be derived from a trigonometric function for values D_y, D_a, and d as the following:

$$\phi = \sin^{-1}\left(\frac{D_y \cdot d + D_a\sqrt{D_a^2 - D_y^2 + d^2}}{D_a^2 + d^2}\right). \tag{13}$$

In this equation, the vertical distance D_y is calculated by adding the half of the vertical displacement δ to the initial distance D_{yi}, and the distance D_a between points B and C is calculated by the addition of the loading arm length L and the initial radius of midplane r_m which is the average of r_i and r_o,

$$D_y = D_{yi} + \frac{\delta}{2}, \quad D_a = L + \frac{\mathrm{r_i} + \mathrm{r_o}}{2}. \tag{14}$$

Taking into consideration such a large deformation, the deformed radii at failure can be derived from a measured displacement δ as follows:

$$\text{deformed radius of the midplane} : r_m' = \frac{D_y - L \cdot \cos\phi - d \cdot \sin\phi}{\sin\phi}, \tag{15}$$

$$\text{deformed inner radius} : r_i' = r_m' - \frac{t}{2}, \tag{16}$$

$$\text{deformed outer radius} : r_o' = r_m' + \frac{t}{2}. \tag{17}$$

For the geometry modifications, the accurate moment M_a can be calculated by substituting the values, ϕ, r_i' and r_o', obtained respectively from Equation (13), (16), and (17) into the Equation (10). In this analytical procedure, the displacement δ measured by the universal loading machine is a significant value in order to calculate the stress distribution appropriately.

3.2. *Finite element analysis*

Figure 7 illustrates a 2D finite element model conducted on the curved beam specimen to verify the relationship between load and displacement as well as the stress distribution in a curved section. Because of the symmetric geometry, only half of the model was enough for analysis, and the symmetric plane was constrained for y direction. The force applied to the loading fixture was straight parallel to the y direction. And, the specimen was fixed to the loading fixture at the contact face on both sides. Abaqus 6.11 supported the analysis, in which plane strain was assumed and material directions 1, 2, and 3 were defined as presented in Figure 7 and the material properties respectively along those directions were determined as indicated in Table 2. The direction 1 was parallel to the fiber direction in the specimen, the direction 2 was parallel to the

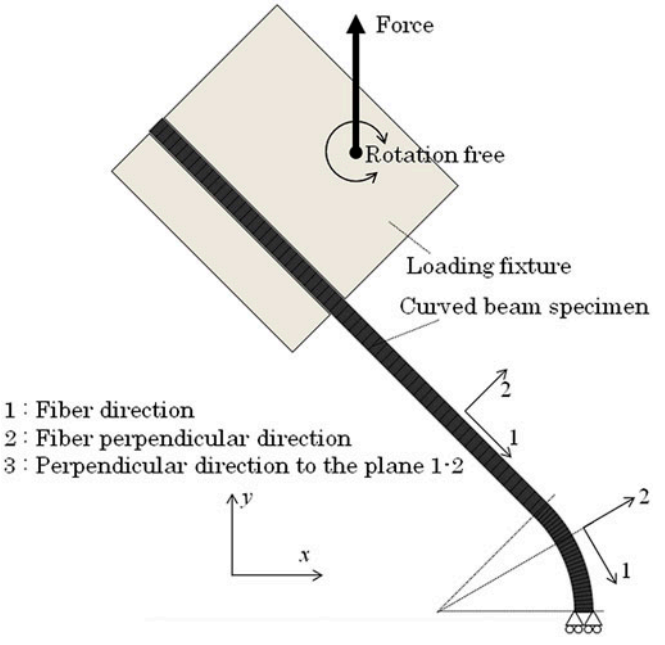

Figure 7. Finite element model.

Table 2. Material properties used in FEA.

Material properties		Unidirectional CF/PP
Elastic modulus (GPa)	E_1	96.5
	E_2	2.9
	E_3	2.9
	G_{12}	1.1
	G_{13}	1.1
	G_{23}	0.91
Poisson's ratio	v_{12}	0.26
	v_{13}	0.26
	v_{23}	0.59

thickness of the curved beam, in other words perpendicular to the fiber direction, and the direction 3 was perpendicular to the plane 1-2. The effect of nonlinearity was considered due to large deformation and all of elements were four-noded quadrilateral with 20 elements in the thickness direction on the specimen model.

4. Results and discussion

4.1. Load–displacement relationship

Figure 8 presents the deformed traces of the specimen profile at some loading steps obtained by the finite element analysis. As shown in this figure, the specimen is largely deformed apparently as the curved section moves to the left side and the radius of the curvature increases gradually with the load and displacement increasing.

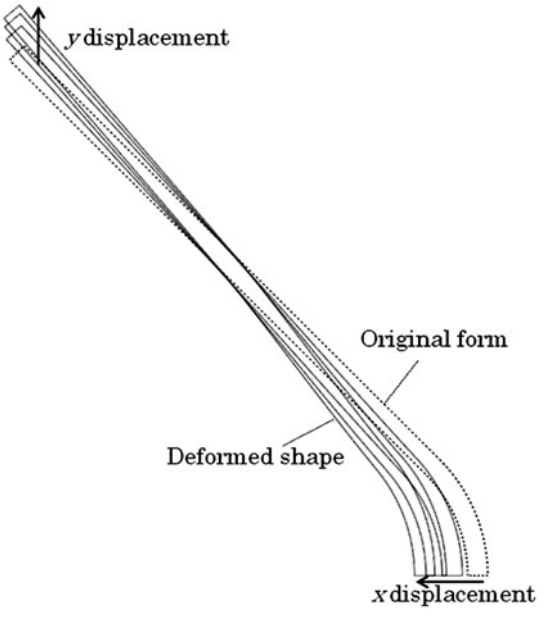

Figure 8. Deformed traces by the finite element analysis.

The load-displacement relationships obtained by the experimental and the FEA results are indicated in Figure 9, where the curves present the experimental results and the plots present the FEA results respectively for three curved geometries. In all of curved geometries, the widths of the specimen are equal to 15 mm. Those curves demonstrate a slight increase in stiffness with the loading force increased. This trend is considered as caused by the decrease of the moment on the curved beam due to the displacement in the x direction as illustrated in Figure 8. Consequently, the finite element analysis shows a satisfying agreement with the experimental result in case of every curved geometry.

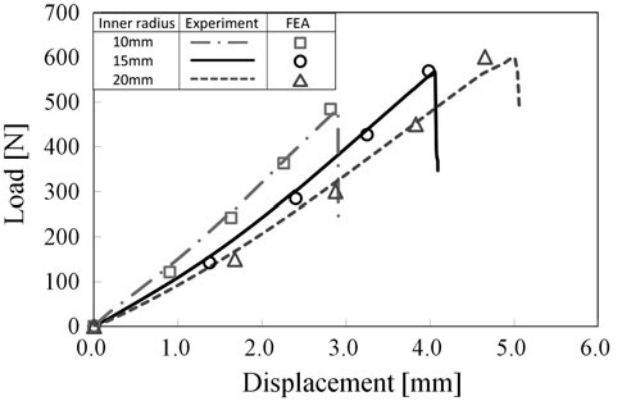

Figure 9. Load-displacement relationships comparing experimental and FEA results.

4.2. Stress distribution at failure force

As each experimental load history has a drop as indicated in Figure 9, every specimen had a significant loss of load and stiffness caused by the failure in the curved section. At the maximum loading force, the failure in the curved section was observed and the strength of the curved section was obtained in each experiment.

An example in case of inner radius 15 mm plotted in a solid line indicates that the failure loading force is approximately obtained 569 N and the failure displacement is 4.05 mm. In Figure 10, the radial stress distribution σ_r and the tangential stress distribution σ_θ at the failure force of 569 N calculated by FEA are displayed as contour figure. These figures indicate that the highest stress area in each case of the radial or tangential direction is on the symmetry plane of curved section where $\theta = \phi$ as mentioned in Equation (11).

Figure 11(a) and (b) indicate respectively the radial and tangential stress distributions on the symmetry plane of the curved section at failure when the force is 570 N and the displacement is 4.05 mm in case of $r_i = 15$ mm. The horizontal axis shows the normalized radial distance $(r - r_i)/t$, ranging from the inner surface to the outer surface

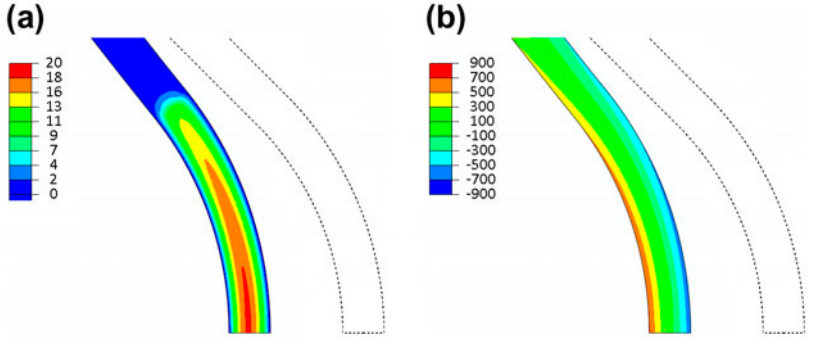

Figure 10. Stress distribution by FEA (a) radial stress : σ_r, (b) tangential stress: σ_θ.

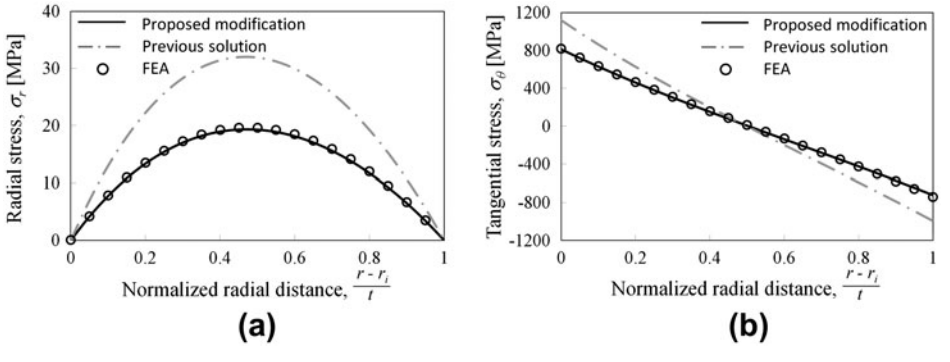

Figure 11. Comparison of analytical and FEA stress distributions on the symmetry plane at failure in case of $r_i = 15$ mm – (a) radial stress and (b) tangential stress.

of the curved section. Those graphs compare the proposed modified solution to the previous solution and the finite element results. The results from the proposed modified solution well fit in the finite element results in relation to both of the radial and tangential stress distributions. In contrast, the results from the previous solution are overestimating the stress value. Therefore, the proposed modified solution by taking into consideration the geometry modification expressed in Equation (13)–(17) has some validity for estimating the analytical stress distribution in thin-curved section, while the previous solution without the geometry modification has no validity.

4.3. Fracture behavior and strength

Three specimens in each case of inner radius, 10, 15 or 20 were investigated for the variation of the fracture behavior and strength. Some assumed fracture pattern was observed from every test result as indicated in Figure 12. The curved beam specimen with the inner radius 10 mm generated an interlaminar fracture in the curved section as shown in Figure 12(a). On the other hand, the specimen with the inner radius 15 mm or 20 mm generated a compressive fracture on the outer surface of the curved section as shown in Figure 12(b) and (c).

From the interlaminar failure observed in every case of r_i=10 mm and the stress analysis by the proposed modified solution, taking an example from Figure 11(a), the interlaminar tensile strength of the thin-curved laminate was obtained around 22 MPa as almost maximum of the radial stress in the curved section calculated by the failure load and displacement. Figure 13 shows a comparison of the calculated interlaminar tensile strengths by three analyses, the previous and modified solutions and the FEA, with each average strength and variation. In a similar way, the compressive strength of the thin-curved laminate was obtained around 720 MPa in case of $r_i = 15$ mm or around 790 MPa in case of $r_i = 20$ mm as the minimum stress in the stress distribution by the modified solution like Figure 11(b). Figure14 shows a comparison of the calculated compressive strengths by three analyses. So, Table 3 presents a summary of the experimental results and the calculated strength values at each fracture pattern for three types of analysis.

4.4. Effect of the material property and geometry

From the above-mentioned analysis result, the difference between the deformed angle ϕ and the initial angle ϕ_i obtained from the displacement δ is significantly sensitive to the evaluated stress. So, the more appropriately evaluated angle ϕ, which should be equal to the actual angle of loading arm from vertical at the end of the curved section, makes it possible to improve the accuracy of the evaluated stress and strength. For an example in case of $r_i = 20$ mm, Figure 15 indicates how much the accuracy of the calculated rotation angle $d\phi$, which subtracts the evaluated angle ϕ from the initial angle ϕ_i, influences the evaluated compressive strength obtained by the modified solution. This relationship means that 1 degree error produces about 5% error of strength.

Such a influence reflects in the difference of the evaluated compressive strength between the modified solution and the FEA in case of $r_i = 20$ mm, which is more than in case of $r_i = 15$ mm as indicated in Figure 14 and Table 3, because the modified solution does not take into account the actual bending deformation of loading arms which increases when the radius of the curved section increases and the thickness decreases. Figure 16 shows the geometric relationship considering the bending

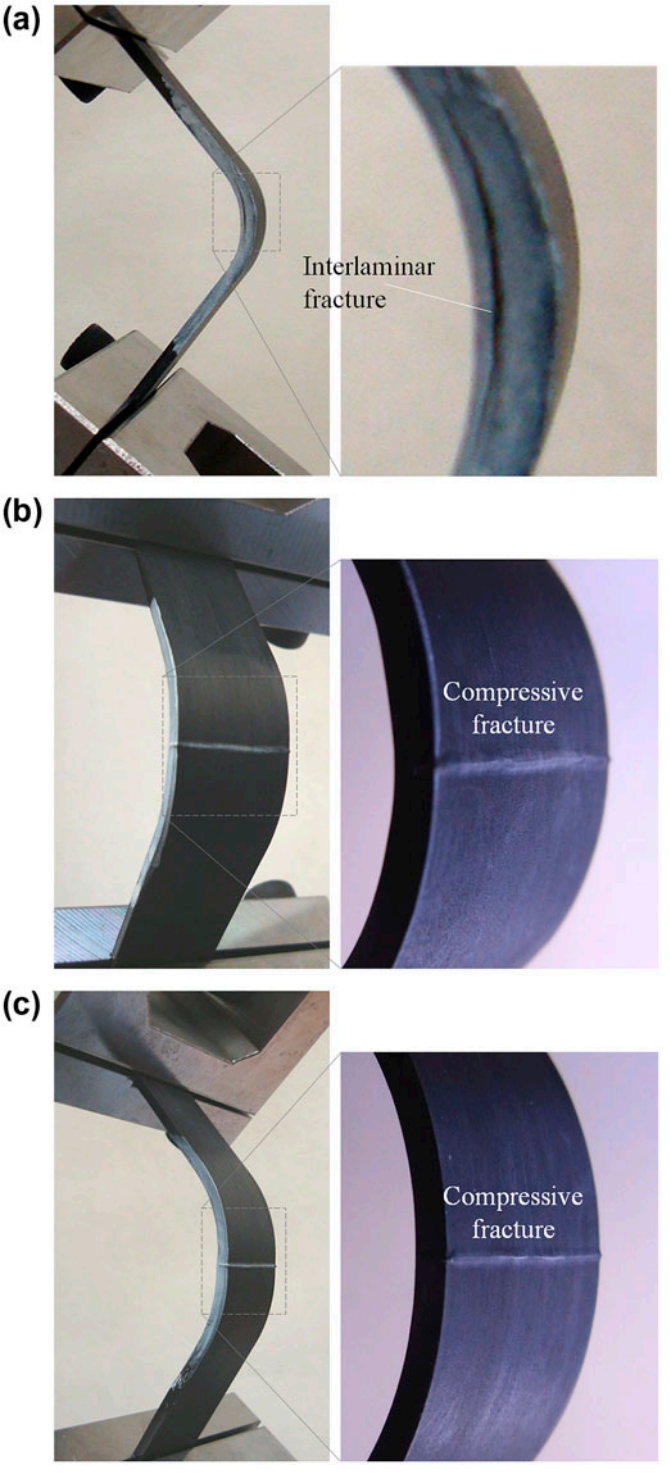

Figure 12. Damaged specimens with magnified images of damaged section (a) $r_i = 10$ mm, (b) $r_i = 15$ mm, (c) $r_i = 20$ mm.

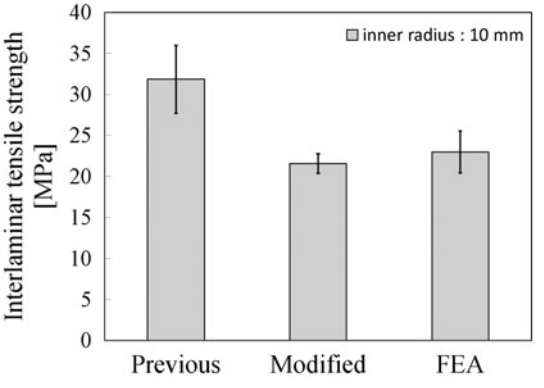

Figure 13. Comparison of interlaminar tensile strengths at failure in case of $r_i = 10$ mm.

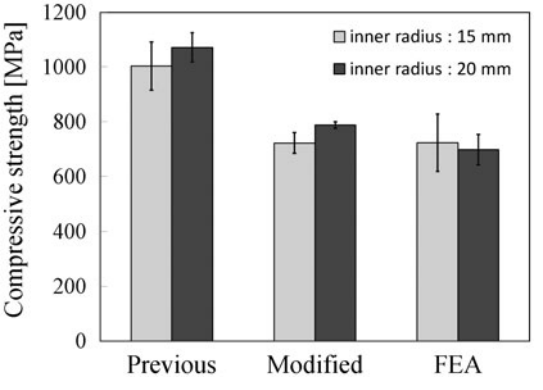

Figure 14. Comparison of compressive strengths at failure in case of $r_i = 15$ mm and 20 mm.

deformation of the arm. For easy understanding and easy calculation, the figure assumes the curved section as a partial linear beam of the extended loading arm, the point B on the extended line as fixed and the loading point as horizontal free while loading. In this way, the deformed arm is illustrated as a bending curve connecting the point B, D′, E′, and C′ in Figure 16. So, the real angle ϕ' of the deformed arm from vertical at the end of the curved section, the point D′, can be derived as follows:

$$\phi' = \phi_i - \varphi. \tag{18}$$

Here, the angle φ is a deflection angle of the arm at the point D′ (or D as the initial point), and from the fundamental bending beam theory is expressed as the following equation,

$$\varphi = \frac{6 \cdot F \cdot \sin \phi_i}{E_\theta \cdot b \cdot t^3} \{(D_a - d)^2 - (L - d)^2\}. \tag{19}$$

Table 3. Experimental results and calculations for interlaminar or compressive stress at failure.

		Experimental value				Interlaminar tensile strength, σ_r^T [MPa]			Compressive strength, σ_θ^C [MPa]		
Test no	Original inner radius, r_i [mm]	Failure force, F_{fail} [N]	Failure Disp., d_{fail} [mm]	Fracture behavior	Fracture location, normalized radial distance, $\frac{r-r_i}{t}$	Previous solution	Modified solution	FEA	Previous solution	Modified solution	FEA
1	10	485	2.90	Interlaminar	0.3	36.5	23.7	25.6	unknown		
2		379	2.41	Interlaminar	0.3	28.5	20.2	21.1			
3		407	2.66	Interlaminar	0.3	30.6	20.8	22.3			
Ave.						31.8	21.6	23.0			
4	15	569	4.05	Compression	1.0	unknown			994	722	741
5		556	3.99	Compression	1.0				971	711	687
6		598	4.35	Compression	1.0				1045	734	742
Ave.									1003	722	723
7	20	601	4.99	Compression	1.0	unknown			1139	823	721
8		594	4.94	Compression	1.0				1125	817	727
9		502	4.39	Compression	1.0				951	724	646
Ave.									1072	788	698

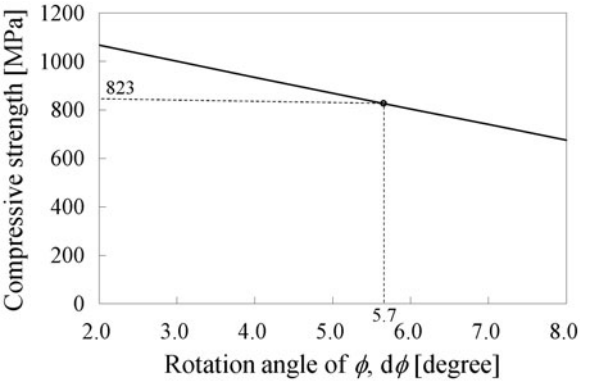

Figure 15. Geometric relationship of the loading arm with bending deformation.

As is clearly seen from Figure 16, the angle ϕ from the modified solution should be less than the actual angle ϕ' as the following,

$$\phi < \phi'. \tag{20}$$

From Equations (18) and (20), the evaluated angle φ should satisfy the following relationship,

$$\varphi < \phi_i - \phi = d\phi. \tag{21}$$

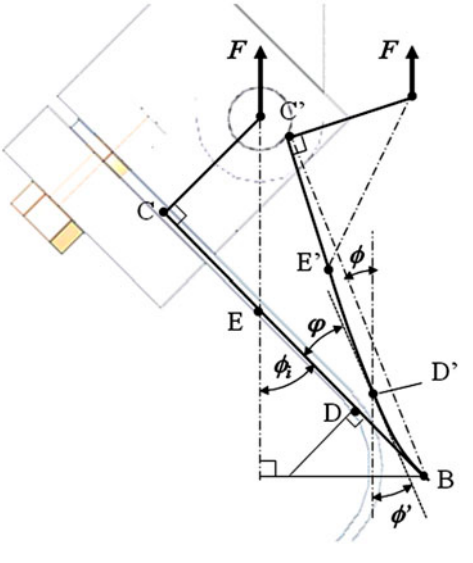

Figure 16. Relationship between the rotation angle of ϕ and the compressive strength in case of $r_i = 20$ mm.

In case of the relationship as an example of Figure 16 (Test No. 7 in Table 3), the rotation angle $d\phi$ between ϕ_i and ϕ is 5.7° from Equation (13), while the bending deflection angle φ is 7.8° from Equation (19). Their calculated values do not satisfy the relationship of Equation (21), so have no validity. For that reason, if φ decreases less than $d\phi$ by increasing the specimen width b, the evaluated value from the modified solution using the test result has potential to satisfy the condition expressed in Equation (21).

In this study, the relatively thin-curved laminate is investigated, so it is not so important to clarify the out-of-plane stiffness as represented by the parameter E_r. Figure 17 shows a parameter study about the influence of the variable radial modulus E_r to the evaluated strength in case of $r_i = 10$ mm. Clearly from this analysis, the evaluated value from the modified solution does not depend so much on the out-of-plane stiffness.

The aim of this study is to evaluate the tangential strength as well as the interlaminar tensile strength of the curved surface by using a thin-curved laminate as mentioned in the introduction. Therefore, it is helpful to investigate how much thickness of the curved laminate is useful for applying the modified solution. Figure 18 shows the relationship between the thickness and the ratio of the maximum compressive stress (the absolute value of the minimum tangential stress) to the maximum interlaminar tensile stress (the maximum radial stress) at a certain loading force obtained from Equation (11), and compares the modified solution with the previous solution. In the modified solution, the variable displacement δ is assumed to be inversely proportional to the cube of the thickness and is calculated referring to the measured displacement from the test result when the thickness is 2 mm.

When the thickness increases, or not to mention the loading force is low, the modified solution is approaching to the previous solution because the displacement δ is coming close to zero. And it is also found that the ratio of the maximum compressive stress to the maximum interlaminar tensile stress decreases with the increase of the thickness. So, whether the ratio is more than ${\sigma_\theta}^C/{\sigma_r}^T$ (the ratio of the compressive strength divided by the interlaminar tensile strength) or not, the failure pattern changes. Because the strength ratio ${\sigma_\theta}^C/{\sigma_r}^T$ can be obtained as 33 from the test results explained in Section 4.3, the thickness borderline between the compressive failure and the interlaminar failure is found as 1.6 mm with $r_i = 10$ mm or 2.1 mm with $r_i = 15$ mm. This

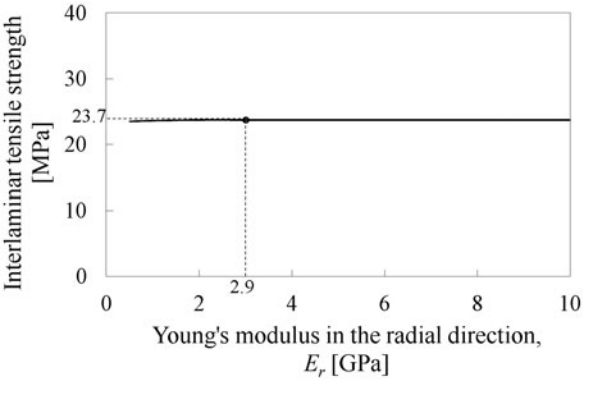

Figure 17. Relationship between the modulus in the radial direction E_r and the interlaminar strength in case of $r_i = 10$ mm.

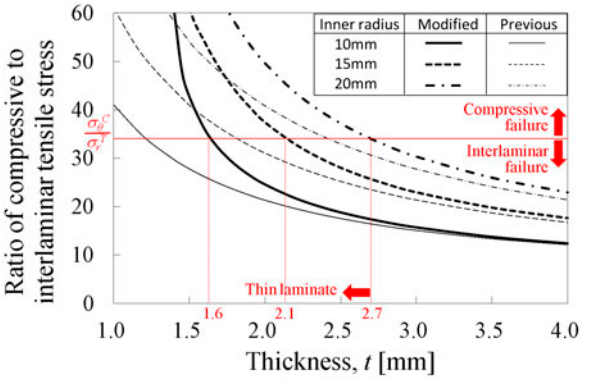

Figure 18. Effects of the thickness and the difference between the modified and the previous solution.

means that if the thickness ranges from 1.6 mm to 2.1 mm, the curved laminate with $r_i = 10$ mm generates the interlaminar failure and the curved laminate with $r_i = 15$ mm generates the compressive failure. Of course, it depends on the material strength related to $\sigma_\theta{}^C/\sigma_r{}^T$. On the other hand, the previous solution just using thicker curved laminate than 2.1 mm with $r_i = 15$ mm satisfies the condition for evaluating only the interlaminar strength. The relationship as indicated in Figure 18 has an effective guideline for designing a curved geometry, related to the thickness and the radius, taking into consideration the elastic deformation.

5. Conclusion

Thin-curved beam specimens formed from unidirectional CF/PP laminates were investigated for verifying the compressive strength as well as the interlaminar tensile strength and the relationship between the curved geometry and the fracture behavior in the curved section. In the process of analysing the stress distribution in the curved section, the geometrical large deformation is a key factor of modifying the conventional analytical stress solution. So, the geometric modified solution was proposed and recognized as an available solution by comparing to the finite element analysis which satisfies the agreement with the experimental load-displacement results. Based on these results, the fracture behavior and strength of the curved section were estimated from the geometric parameters related to the stress distribution calculated by the proposed modified solution. That is to say, the curved laminate with the thickness decreasing or the inner radius increasing has a tendency to generate the compressive fracture on the curved surface. In contrast, the curved laminate with the thickness increasing or the inner radius decreasing has a tendency to generate the interlaminar fracture in the curved section. Those experimental procedures and evaluating methods will contribute toward a technique applied to designing and manufacturing a variety of laminated composite structures with thin curvature.

Acknowledgments

A part of this work belongs to Japanese METI-NEDO project ‘Development of sustainable hyper composite technology’ since 2008fy. The authors gratefully acknowledge the support of this study by all of concerned participators in the project.

References

[1] Vaidya UK, Chawla KK. Processing of fibre reinforced thermoplastic composites. Int. Mater. Rev. 2008;53:185–218.
[2] Nomra T, Nishio T, Sato H, Sano H. Study of super olefine polymer by the control of nano-order structure. IV. Structure of super olefine polymer. Kobunshi Ronbunshu. 1993;50:87–91.
[3] Hayashi T, Sasaki A, Terasawa T, Akiyama K. Study on interfacial adhesion between carbon fiber thermoplastic resin and mechanical properties of the composite. in: Proceedings 11th Japan International SAMPE Symposium & Exhibition (JISSE-11), Tokyo; 2009.
[4] Yamauchi M, Kan Y, Ohsawa I, Uzawa K, Takahashi J. Improvement of interfacial shear strength between carbon fiber and polypropylene. in: Proceedings. 11th Japan International SAMPE Symposium & Exhibition (JISSE-11), Tokyo; 2009.
[5] Matsuo T, Takahashi J, Uzawa K, Yamane M. New design approach for high stiffness and high impact-absorbing structure by carbon fiber reinforced thermoplastic composites. in: Proc. 15th European Conference on Composite Material (ECCM-15), Venice; 2012.
[6] Kedward KT, Wilson RS, Mclean SK. Flexure of simply curved composite shapes. Composites. 1989;20:527–536.
[7] Feih S, Shercliff HR. Quality assessment of curved composite components in peel joint structures. Composites Part A. 2005;36:397–408.
[8] Olsson R. A survey of test methods for multiaxial and out-of-plane strength of composite laminates. Compos. Sci. Technol. 2011;71:773–783.
[9] Lagace PA, Weems DB. A through-the-thickness strength specimen for composites. Test Methods for Des. Allowables for Fibrous Compos. ASTM STP1003. 1989;2:197–207.
[10] Jackson WC, Martin RH. An interlaminar tension strength specimen. Test. Des., ASTM STP1206. 1993;11:333–354.
[11] Jackson WC, Ifju PG. Through-the-thickness tensile strength of textile composites. Test. Des. ASTM STP1274. 1996;218–238.
[12] Hiel CC, Sumich M, Chappell DP. A curved beam test specimen for determining the interlaminar tensile strength of a laminated composite. J. Compos. Mater. 1991;25:854–868.
[13] ASTM D 7291. Standard test method for through-thickness "Flatwise" tensile strength and elastic modulus of a fiber-reinforced polymer matrix composite.
[14] ASTM D 6415. Standard test method for measuring the curved beam strength of a fiber-reinforced polymer-matrix composite.
[15] Hufenbach W, Hornig A, Zhou B, Langkamp A, Gude M. Determination of strain rate dependent through-thickness tensile properties of textile reinforced thermoplastic composites using L-shaped beam specimens. Compos. Sci. Technol. 2011;71:1110–1116.
[16] Shenoi RA, Wang W. Through-thickness stresses in curved composite laminates and sandwich beams. Compos. Sci. Technol. 2001;61:1501–1512.
[17] Hull D, Clyne TW. An introduction to composite materials. 2nd ed. New York (NY): Press Syndicate of the University of Cambridge; 1996.
[18] Lekhnitskii SG. Anisotropic plates. New York, NY: Gordon and Breach Science Publishers; 1968.
[19] Shivakumar KN, Allen HG, Avva VS. Interlaminar tension strength of graphite/epoxy composite laminates. J. AIAA. 1994;32:1478–1484.